

Measurement of the helicity asymmetry E in $\omega \rightarrow \pi^+\pi^-\pi^0$ photoproduction

Z. Akbar,¹³ P. Roy,^{13,*} S. Park,^{13,†} V. Crede,^{13,‡} A. V. Anisovich,^{3,14} I. Denisenko,^{3,26} E. Klempt,^{3,37}
V. A. Nikonov,^{3,14} A. V. Sarantsev,^{3,14} K. P. Adhikari,²⁸ S. Adhikari,¹² M. J. Amarian,³² S. Anefalos Pereira,¹⁹
H. Avakian,³⁷ J. Ball,⁸ M. Battaglieri,²⁰ V. Batourine,³⁷ I. Bedlinskiy,²⁴ S. Boiarinov,³⁷ W. J. Briscoe,¹⁶
J. Brock,³⁷ W. K. Brooks,^{37,38} V. D. Burkert,³⁷ F. T. Cao,¹⁰ C. Carlin,³⁷ D. S. Carman,³⁷ A. Celentano,²⁰
G. Charles,³² T. Chetry,³¹ G. Ciullo,^{11,18} L. Clark,⁴⁰ P. L. Cole,¹⁷ M. Contalbrigo,¹⁸ O. Cortes,¹⁷
A. D'Angelo,^{21,33} N. Dashyan,⁴⁴ R. De Vita,²⁰ E. De Sanctis,¹⁹ A. Deur,³⁷ C. Djalali,³⁵ M. Dugger,²
R. Dupre,²³ H. Egiyan,^{29,37} L. El Fassi,^{1,28} P. Eugenio,¹³ G. Fedotov,^{31,34} R. Fersch,⁹ A. Filippi,²²
A. Fradi,^{23,§} M. Garçon,⁸ N. Gevorgyan,⁴⁴ K. L. Giovanetti,²⁵ F. X. Girod,^{8,37} C. Gleason,³⁵ W. Gohn,^{10,¶}
E. Golovatch,³⁴ R. W. Gothe,³⁵ K. A. Griffioen,⁴³ M. Guidal,²³ L. Guo,^{12,37} K. Hafidi,¹ H. Hakobyan,^{38,44}
C. Hanretty,^{13,37} N. Harrison,³⁷ M. Hattawy,¹ D. Heddle,^{9,37} K. Hicks,³¹ G. Hollis,³⁵ M. Holtrop,²⁹
D. G. Ireland,⁴⁰ B. S. Ishkhanov,³⁴ E. L. Isupov,³⁴ D. Jenkins,⁴¹ S. Joosten,³⁶ C. D. Keith,³⁷ D. Keller,^{31,42}
G. Khachatryan,⁴⁴ M. Khachatryan,³² M. Khandaker,^{30,**} A. Kim,¹⁰ W. Kim,²⁷ A. Klein,³² F. J. Klein,⁷
V. Kubarovsky,³⁷ L. Lanza,²¹ K. Livingston,⁴⁰ I. J. D. MacGregor,⁴⁰ N. Markov,¹⁰ B. McKinnon,⁴⁰
D. G. Meekins,³⁷ T. Mineeva,³⁸ V. Mokeev,^{34,37} A. Movsisyan,¹⁸ C. Munoz Camacho,²³ P. Nadel-Turonski,^{7,37}
S. Niccolai,²³ M. Osipenko,²⁰ A. I. Ostrovidov,¹³ M. Paolone,³⁶ R. Paremuzyan,²⁹ K. Park,^{27,35,37}
E. Pasyuk,^{2,37} W. Phelps,¹² O. Pogorelko,²⁴ J. W. Price,⁴ Y. Prok,^{32,42} D. Protopopescu,⁴⁰ B. A. Raue,^{12,37}
M. Ripani,²⁰ B. G. Ritchie,² A. Rizzo,^{21,33} G. Rosner,⁴⁰ F. Sabatié,⁸ C. Salgado,³⁰ R. A. Schumacher,⁶
Y. G. Sharabian,³⁷ Iu. Skorodumina,^{34,35} G. D. Smith,³⁹ D. I. Sober,⁷ D. Sokhan,^{39,40} N. Sparveris,³⁶
S. Stepanyan,³⁷ I. I. Strakovsky,¹⁶ S. Strauch,³⁵ M. Taiuti,^{15,20} M. Ungaro,^{10,37} H. Voskanyan,⁴⁴
E. Voutier,²³ X. Wei,³⁷ M. H. Wood,^{5,35} N. Zachariou,³⁹ L. Zana,^{29,39} J. Zhang,^{32,42} and Z. W. Zhao^{32,35}

(The CLAS Collaboration)

¹Argonne National Laboratory, Argonne, Illinois 60439

²Arizona State University, Tempe, Arizona 85287-1504

³Helmholtz-Institut für Strahlen- und Kernphysik, Universität Bonn, 53115 Bonn, Germany

⁴California State University, Dominguez Hills, Carson, CA 90747

⁵Canisius College, Buffalo, NY

⁶Carnegie Mellon University, Pittsburgh, Pennsylvania 15213

⁷Catholic University of America, Washington, D.C. 20064

⁸IRFU, CEA, Université Paris-Saclay, F-91191 Gif-sur-Yvette, France

⁹Christopher Newport University, Newport News, Virginia 23606

¹⁰University of Connecticut, Storrs, Connecticut 06269

¹¹Università di Ferrara, 44121 Ferrara, Italy

¹²Florida International University, Miami, Florida 33199

¹³Florida State University, Tallahassee, Florida 32306

¹⁴NRC "Kurchatov Institute", PNPI, 188300, Gatchina, Russia

¹⁵Università di Genova, Dipartimento di Fisica, 16146 Genova, Italy

¹⁶The George Washington University, Washington, DC 20052

¹⁷Idaho State University, Pocatello, Idaho 83209

¹⁸INFN, Sezione di Ferrara, 44100 Ferrara, Italy

¹⁹INFN, Laboratori Nazionali di Frascati, 00044 Frascati, Italy

²⁰INFN, Sezione di Genova, 16146 Genova, Italy

²¹INFN, Sezione di Roma Tor Vergata, 00133 Rome, Italy

²²INFN, Sezione di Torino, 10125 Torino, Italy

²³Institut de Physique Nucléaire, CNRS/IN2P3 and Université Paris Sud, Orsay, France

²⁴Institute of Theoretical and Experimental Physics, Moscow, 117259, Russia

²⁵James Madison University, Harrisonburg, Virginia 22807

²⁶Joint Institute for Nuclear Research, 141980 Dubna, Russia

²⁷Kyungpook National University, Daegu 41566, Republic of Korea

²⁸Mississippi State University, Mississippi State, MS 39762-5167

²⁹University of New Hampshire, Durham, New Hampshire 03824-3568

³⁰Norfolk State University, Norfolk, Virginia 23504

³¹Ohio University, Athens, Ohio 45701

³²Old Dominion University, Norfolk, Virginia 23529

³³Università di Roma Tor Vergata, 00133 Rome Italy

³⁴Skobeltsyn Institute of Nuclear Physics, Lomonosov Moscow State University, 119234 Moscow, Russia

³⁵University of South Carolina, Columbia, South Carolina 29208

³⁶Temple University, Philadelphia, PA 19122

³⁷Thomas Jefferson National Accelerator Facility, Newport News, Virginia 23606

³⁸Universidad Técnica Federico Santa María, Casilla 110-V Valparaíso, Chile

³⁹Edinburgh University, Edinburgh EH9 3JZ, United Kingdom

⁴⁰University of Glasgow, Glasgow G12 8QQ, United Kingdom

⁴¹Virginia Tech, Blacksburg, Virginia 24061-0435

⁴²University of Virginia, Charlottesville, Virginia 22901

⁴³College of William and Mary, Williamsburg, Virginia 23187-8795

⁴⁴Yerevan Physics Institute, 375036 Yerevan, Armenia

(Dated: Received: February 15, 2022/ Revised version:)

The double-polarization observable E was studied for the reaction $\gamma p \rightarrow p\omega$ using the CEBAF Large Acceptance Spectrometer (CLAS) in Hall B at the Thomas Jefferson National Accelerator Facility and the longitudinally-polarized frozen-spin target (FROST). The observable was measured from the charged decay mode of the meson, $\omega \rightarrow \pi^+\pi^-\pi^0$, using a circularly-polarized tagged-photon beam with energies ranging from the ω threshold at 1.1 to 2.3 GeV. A partial-wave analysis within the Bonn-Gatchina framework found dominant contributions from the $3/2^+$ partial wave near threshold, which is identified with the sub-threshold $N(1720)3/2^+$ nucleon resonance. To describe the entire data set, which consisted of ω differential cross sections and a large variety of polarization observables, further contributions from other nucleon resonances were found to be necessary. With respect to non-resonant mechanisms, π exchange in the t -channel was found to remain small across the analyzed energy range, while pomeron t -channel exchange gradually grew from the reaction threshold to dominate all other contributions above $W \approx 2$ GeV.

PACS numbers: 13.60.Le, 13.60.-r, 14.20.Gk, 25.20.Lj

I. INTRODUCTION

The production of light vector mesons (ρ^0 , ω , ϕ) in electromagnetically-induced reactions off the nucleon has attracted interest recently due to the availability of high-quality data sets from experiments that study baryon resonances, e.g. at Jefferson Laboratory (JLab), the Electron Stretcher Accelerator (ELSA), and the Mainz Microtron (MAMI). An experimental program that focuses on the photoproduction of vector mesons at 9 GeV is planned at JLab using the GlueX detector [1]. The three lowest-mass vector mesons have the same $J^{PC} = 1^{--}$ quantum numbers as the photon. For this reason, the photoproduction of these mesons at very high energies, $E_\gamma > 20$ GeV, can successfully be described as a diffractive process: The photon converts to a vector meson, which then scatters off the proton by the exchange of pomerons. These virtual colorless objects carry no charge and share the $J^{PC} = 0^{++}$ quantum numbers of the vacuum [2].

At medium energies, $4 < E_\gamma < 20$ GeV, pomeron exchange is not sufficient to describe the existing data, e.g. from SLAC [3], Cornell [4], Daresbury [5], and the exchange of additional Regge families is needed, see e.g. the discussion in Ref. [6]. The comparison between

ρ and ω data presented in Ref. [7] indicated that meson-exchange contributions become important in ω photoproduction. Pion exchange is generally expected to dominate over unnatural exchanges, whereas the importance of tensor exchange, which is mediated by the f_2 and a_2 mesons, is *a priori* unknown. The authors of Ref. [7] found that in order to describe the data, a smooth transition was required between the meson-exchange model at lower energies, $E_\gamma < 5$ GeV, and Regge theory at high energies, $E_\gamma > 20$ GeV. They suggested that the dominant contributions come from π^0 and f_2 -meson exchanges.

Close to the ω photoproduction threshold in the baryon resonance regime, N^* states strongly contribute to ω production. The contributions of twelve N^* resonances, along with their $N^* \rightarrow p\omega$ branching ratios, have been determined within the Bonn-Gatchina (BnGa) coupled-channels partial-wave analysis (PWA) using data from the CBELSA/TAPS experiment [8]. The dominant contribution near threshold was found to be the $3/2^+$ partial wave, which was primarily identified with the sub-threshold $N(1720)3/2^+$ resonance. The dominance of that partial wave near threshold is surprising since such behavior implies that the decay into ωN proceeds via orbital angular momentum $L = 1$. The contributions from the $1/2^-$ and $3/2^-$ partial waves were notably smaller, in spite of the fact that the ωN channel could couple to these partial waves with $L = 0$. A significant $3/2^+$ amplitude at low energies was also observed in a recent CLAS single-channel PWA, but the authors did not claim any specific resonance contributions owing to the complex structure of the $3/2^+$ wave [9]. Notable contributions from the $5/2^+$ partial wave were reported in both analyses [8, 9]. A structure above $W = 2$ GeV has been identified with the $N(2000)5/2^+$ state. An improved quark model approach to ω -meson photoproduction with an ef-

* Present address: University of Michigan, Ann Arbor, MI 48109

† Present address: Korea Atomic Energy Research Institute, Gyeongju-si, 38180, South Korea

‡ Corresponding author: crede@fsu.edu

§ Present address: Faculty of Sciences of Gabes, Department of Physics, 6072-Gabes, Tunisia

¶ Present address: University of Kentucky, Lexington, KY 40506

** Present address: Idaho State University, Pocatello, Idaho 83209

fective Lagrangian was presented in Ref. [10], where the two resonances, $N(1720) 3/2^+$ and $N(1680) 5/2^+$, were observed to dominate over other excited states.

The isoscalar nature of the ω meson ($I = 0$) facilitates the search for nucleon resonances. The photoproduction of the ω in s -channel processes can only proceed via N^* states with $I = \frac{1}{2}$; no contributions from Δ^* resonances with $I = \frac{3}{2}$ are allowed.

In this paper, we report data obtained for the double-polarization observable known as the helicity asymmetry E for the reaction $\gamma p \rightarrow p\omega$, where the ω was identified through detection of its decay products $\pi^+\pi^-\pi^0$. The data reported here cover an incident photon energy range E_γ from 1.1 up to 2.3 GeV, and show (almost) the full angular coverage. The observable E was measured using a circularly-polarized photon beam and a longitudinally-polarized proton target. The polarized cross section for this configuration is given by

$$\sigma = \sigma_0 (1 - \Lambda_z \delta_\odot E), \quad (1)$$

where σ_0 is the unpolarized cross section, δ_\odot denotes the degree of circular photon-beam polarization, Λ_z is the degree of longitudinal target-proton polarization, and E is defined as:

$$\Lambda_z \delta_\odot E = \frac{\sigma_{1/2} - \sigma_{3/2}}{\sigma_{1/2} + \sigma_{3/2}} = \frac{\sigma_{1/2} - \sigma_{3/2}}{\sigma_0}, \quad (2)$$

where $\sigma_{1/2}$ and $\sigma_{3/2}$ are the helicity-dependent cross sections with photon and nucleon spins anti-aligned and aligned, respectively.

This paper has the following structure. A brief summary of previous measurements in ω photoproduction is presented in Sec. II. Section III gives an introduction to the CLAS-g9a (FROST) experimental setup. The data reconstruction and event selection is discussed in Sec. IV and the extraction of the polarization observable is described in Section V. Finally, the experimental results and a discussion of the observed resonance contributions are presented in Secs. VI and VII.

II. PREVIOUS MEASUREMENTS

Cross section data for the reaction $\gamma p \rightarrow p\omega$ were obtained and studied at many different laboratories over a wide kinematic range [11–15]. A review of the main data sets published before 2013 and a corresponding comparison of their coverage in energy and solid angle can be found in Ref. [16]. The total cross section for ω photoproduction reaches about $8.5 \mu\text{b}$ and exhibits a pronounced peak structure at about $E_\gamma = 1.3 \text{ GeV}$ in addition to a broader peak at about $E_\gamma = 1.9 \text{ GeV}$ [14], similar in shape to that seen in ρ and ϕ production. The differential cross sections, $d\sigma/dt$, show an exponential fall-off at small values of the squared recoil momentum, t .

Few measurements exist for polarization observables in ω photoproduction. The photon-beam asymmetry Σ was

first measured by the GRAAL Collaboration in 2006 from the decay modes $\omega \rightarrow \pi^0\gamma$ and $\omega \rightarrow \pi^+\pi^-\pi^0$, and was presented in four energy bins that cover an energy range from threshold up to a photon energy of 1.5 GeV [12]. A second measurement based on both decay modes was published in 2015 and showed improved angular coverage [17]. The photon-beam asymmetry Σ was also measured by the CBELSA/TAPS Collaboration for a maximum energy of $E_\gamma = 1.5 \text{ GeV}$ [18]. We refer to Refs. [19, 20] prepared by the CLAS Collaboration for a detailed discussion of Σ_ω including new high-statistics data from Jefferson Lab [20].

The first measurements of ω double-polarization observables were reported from the CBELSA/TAPS Collaboration [21]. The publication provided five data points for the observable G at a single energy interval of $1108 < E_\gamma < 1300 \text{ MeV}$ and the helicity asymmetry, E , for a photon energy range from close to threshold at $E_\gamma = 1108 \text{ MeV}$ to $E_\gamma = 2300 \text{ MeV}$. Both measurements cover the full solid angle.

Decays of vector mesons give rise to additional spin observables beyond those accessed in pseudoscalar meson decays, and vector-meson decays provide the opportunity to access spin-density matrix elements (SDMEs). High-statistics results on SDMEs, ρ_{00}^0 , ρ_{10}^0 , and ρ_{1-1}^0 , have already been measured at CLAS [13] (for $E_\gamma < 3.8 \text{ GeV}$) and CBELSA/TAPS [14] (for $E_\gamma < 2.5 \text{ GeV}$) using an unpolarized photon beam, and CBELSA/TAPS [14] also reported the first measurements of polarized SDMEs (ρ_{00}^1 , ρ_{11}^1 , $\text{Re } \rho_{10}^1$, and $\text{Im } \rho_{1-1}^1$), using a linearly-polarized photon beam for $E_\gamma < 1.65 \text{ GeV}$.

III. EXPERIMENTAL SETUP

The experiment was performed at the Continuous Electron Beam Accelerator Facility (CEBAF) at Jefferson Lab using the CEBAF Large Acceptance Spectrometer (CLAS) [22] in Hall B with a circularly-polarized, tagged, bremsstrahlung photon beam whose helicity state was changed pseudo-randomly at a rate of 29.560 Hz. The measurements were part of the “g9a” running period, which were the first measurements using the Jefferson Lab “frozen spin” target FROST [23] described below. A circularly-polarized photon beam results from a polarization transfer when the incident electron beam itself is longitudinally polarized. The electron beam polarization was determined with the Hall B Møller polarimeter [25] that measured the asymmetry in elastic electron-electron (Møller) scattering. The data for the double-polarization observable E were recorded in seven different groups of runs defined by the target-proton polarization and two different accelerator energies with electron-beam polarization degrees, δ_{e-} , of 84.8% and 83.0%, respectively; the uncertainty in the degree of electron-beam polarization was about 1.4% [22].

The longitudinally-polarized electron beam was extracted from the CEBAF accelerator and was incident

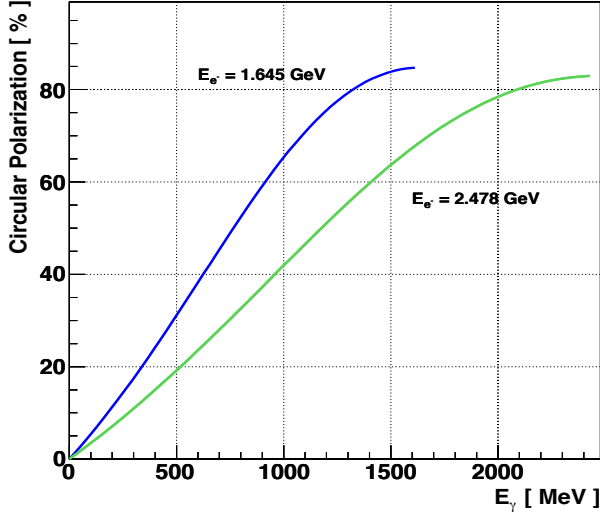


FIG. 1. (Color online) Degree of circular-photon polarization as a function of photon energy for the two CEBAF energies of 1.645 GeV (blue) and 2.478 GeV (green).

on the thin radiator of the Hall B photon tagger [26]. The photon tagging system included a focal plane incorporating a layer of 384 partially overlapping small scintillators that detected electrons that had undergone bremsstrahlung; the small scintillators thus provided the photon-beam energy definition and resolution via energy conservation. A second layer of 61 larger scintillators provided the timing resolution for an event through a coincidence of an electron passing through one of the larger scintillators with the detection of decay products following meson photoproduction as described below.

In this experiment, the tagging system produced circularly-polarized tagged photons in the energy range between $E_\gamma = 0.35$ and 2.37 GeV with an energy resolution of $\sim 10^{-3} E_{e-}$. The degree of circular polarization of the bremsstrahlung photons, δ_\odot , was determined from the polarization transfer of the longitudinally-polarized electrons [24]:

$$\delta_\odot = \delta_{e-} \cdot \frac{4x - x^2}{4 - 4x + 3x^2}, \quad (3)$$

where $x = E_\gamma/E_{e-}$, and E_γ as well as E_{e-} are the energy of the incoming photon and the energy of the electron beam, respectively. Figure 1 shows that the degree of the circular photon-beam polarization is roughly proportional to the photon-beam energy.

The charged particles in the $p\pi^+\pi^-\pi^0$ final state were detected in the CLAS spectrometer, which provided a large coverage for charged particles in the polar-angle range $8^\circ < \theta_{\text{lab}} < 135^\circ$. The four-momentum vectors of the particles were reconstructed from their tracks in the toroidal magnetic field of the spectrometer by a set of three drift-chamber packages [27] and by particle identification using time-of-flight information from plastic scin-

tillators located about 5 m from the target [28]. The CLAS spectrometer provided a momentum and angle resolution of $\Delta p/p \approx 1\%$ and $\Delta\theta \approx 1^\circ$ - 2° , respectively. A set of plastic scintillation counters close to the target provided event start times [29]. For this experiment, coincident signals from the photon tagger, start-, and time-of-flight counters constituted the event trigger that required a coincidence between a scattered-electron signal from the photon tagger and at least one charged track in CLAS. More details on the spectrometer can be found in Ref. [22].

Data from reactions using the FROzen Spin Target (FROST) [23] at the center of the CLAS spectrometer were accumulated. The target material consisted of frozen beads of butanol ($\text{C}_4\text{H}_9\text{OH}$) that were 1-2 mm in diameter. Approximately 5 g of these beads were loaded into a cylindrical target cup with a diameter of 15 mm and a length of 50 mm. The target was longitudinally polarized with microwaves via Dynamic Nuclear Polarization (DNP) [30] in the bore of a 5 T polarizing (solenoid) magnet outside CLAS at about 200-300 mK. The polarization was maintained at a frozen-spin temperature of about 30 mK inside the spectrometer by a weaker 0.56 T holding field during data taking. The FROST target was typically polarized with an average starting polarization of 84% in the positive-spin state and -86% in the negative. Relaxation times ranged from about 2800 h with

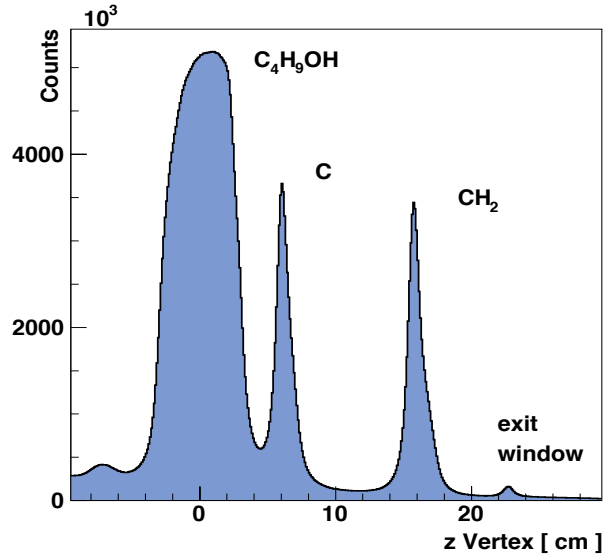


FIG. 2. (Color online) The z -vertex distribution (axis along the beamline) in the FROST-g9a experiment based on about 30% of the total statistics for the full photon energy range. The three peaks for the different targets are clearly visible: butanol, carbon, and polyethylene (from left to right). Also visible are the exit window of the vacuum chamber and an enhancement to the left of the butanol peak where the target cup was attached to a stainless steel tube, which was used to insert the cup into the cryostat.

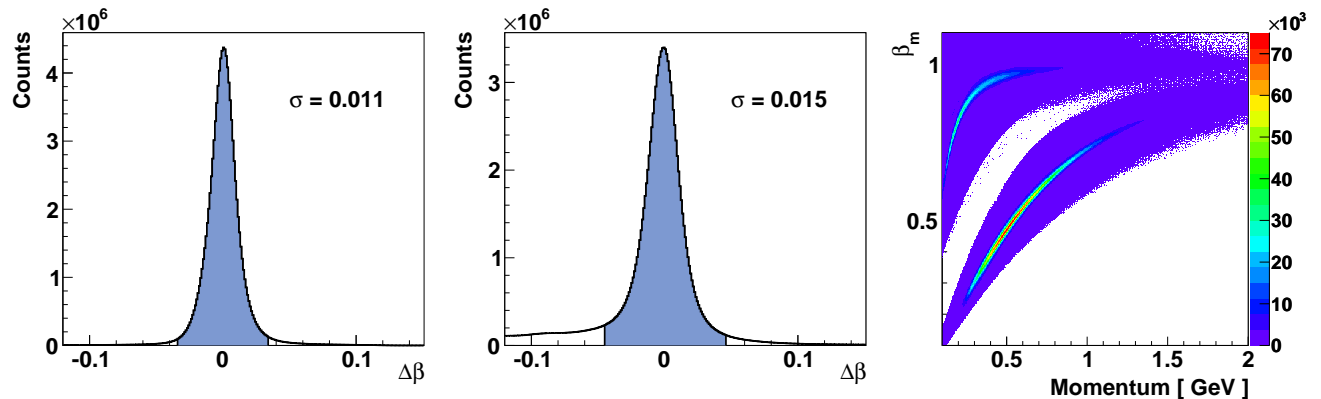


FIG. 3. (Color online) Left and middle: $\Delta\beta = |\beta_c - \beta_m|$ distributions for protons and charged pions, respectively. The blue area indicates the 3σ cuts according to Eq. (4). Right: The distribution of β_m versus particle momentum before the 3σ cuts.

beam on target to about 3600 h without beam. The target relaxed more quickly in the negative spin state, about 1400 h with beam and 1900 h without. The maximum polarization was -94% . The target was re-polarized (and the polarization reversed) about once a week. The design details and the target performance in the FROST experiment are discussed in Ref. [23].

The DNP technique was realized by placing the target material in a high magnetic field under conditions such that the polarization of the free electron spins approached unity. Spin flips of an electron and that of a nearby free proton were induced by microwaves of frequency near the electron spin resonance. Since the nucleon spins couple more weakly with the lattice than the electron spins, their spin-relaxation rates were much longer and the nucleons could accumulate into either the positive or negative spin state without reversing the magnetic field. This could be tuned by the proper microwave frequency. As a result, the direction of the target-proton polarization in this experiment was defined by two quantities: The direction of the proton polarization with respect to the holding magnetic field and the direction of the holding magnetic field with respect to the incident photon-beam polarization plane. The degree of the target-proton polarization was measured during the run with the continuous wave nuclear magnetic resonance (NMR) technique [23].

Data were also simultaneously obtained from two additional targets: a 1.5-mm-thick carbon disk and a 3.5-mm thick CH_2 disk at approximately 6 and 16 cm downstream of the butanol sample, respectively. Figure 2 shows the z -vertex distribution in the FROST-g9a experiment based upon about 30 % of the total statistics. The three dominant peaks for the different targets are clearly visible. The carbon target was used to study background from bound nucleons and to determine dilution factors, whereas the CH_2 target provided relevant information on events off unpolarized nucleons. The thickness of the additional targets was chosen such that the hadronic rate from each was about 10 % the rate of butanol.

IV. PREPARATION OF FINAL STATES

The data presented here were accumulated between November 2007 and February 2008 in seven run periods with CEBAF energies of 1.645 GeV (Periods 1-3) and 2.478 GeV (Periods 4-7). These data were also used to extract the helicity asymmetry for a variety of other final states, see e.g. Refs. [31, 32]. The event reconstruction and selection of the photoproduction channel $\gamma p \rightarrow p\omega \rightarrow p\pi^+\pi^-\pi^0$ is described below and resulted in the reconstruction of 62,300 ω events from the full data set obtained in this experiment.

A. Event reconstruction

The reaction $\gamma p \rightarrow p\pi^+\pi^-(\pi^0)$ was identified in a first step by requiring exactly one proton track and two charged-pion tracks in the CLAS detector. Positively- and negatively-charged pions were distinguished by their track curvatures in the toroidal magnetic field. The acceptance of π^- mesons was smaller than for π^+ mesons since they were bent toward the beamline and a large fraction escaped through the forward hole of the CLAS spectrometer.

Particle identification was then improved by applying a cut on $\Delta\beta$:

$$\Delta\beta = |\beta_c - \beta_m| = \left| \sqrt{\frac{p^2}{m^2 + p^2}} - \beta_m \right| < 3\sigma, \quad (4)$$

where $\beta_m = v/c$ was the empirically-measured value for each particle based on timing information from the time-of-flight and start counter systems, and β_c was determined from the measured momentum using the CLAS drift chambers and the PDG mass [33] for the particle. While the quantity $\Delta\beta$ depends on particle momentum, the $\Delta\beta$ distribution is approximately Gaussian when summed over all β_m values, with width $\sigma = 0.011$

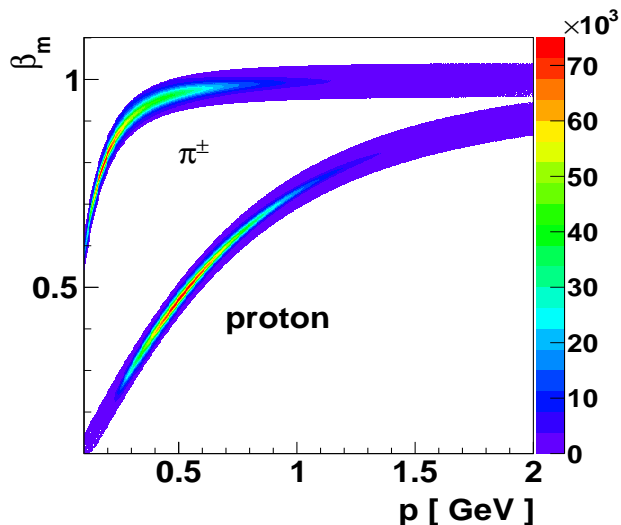


FIG. 4. (Color online) The distribution of β_m versus particle momentum after the 3σ cuts on $\Delta\beta$ according to Eq. (4).

and 0.015 for the proton and pions, respectively. Figure 3 shows the $\Delta\beta$ distributions for protons (left) and charged pions (middle). The tail on the left side of the $\Delta\beta$ peak for pions originates from misidentified electrons. Also shown in Fig. 3 (right) is the distribution of β_m versus particle momentum before the 3σ cuts. The final distribution of β_m versus particle momentum after the 3σ cuts on $\Delta\beta$ according to Eq. (4) is shown in Fig. 4. Clear bands for the proton and the pions are visible.

All detected final-state particles were also corrected for their energy loss along the path from the target to the time-of-flight scintillator array. Moreover, the magnitude of the particle momentum was corrected for small misalignments of the CLAS drift chambers and fluctuations in the toroidal field. These corrections were typically of the order of a few MeV.

All detected final-state particles exhibited small modulations in the laboratory polar and azimuthal angular distributions with amplitudes of $< 0.5^\circ$. These modulations were consistent with effects of the solenoidal holding field on charged particles. The four-momentum for each detected particle was corrected independently in both angles; given the size of the effect, correlations between the two angles were considered negligible. Since the E observable was extracted separately from each of the seven groups of runs without mixing data using different holding field directions, any remaining effect would drop out when the asymmetries were formed.

In a second step, all events were subject to kinematic fitting. Events were tested for energy and momentum conservation in a four-constraint (4C) fit for detected particles and in a one-constraint (1C) fit for a missing π^0 . The exclusive reaction $\gamma p \rightarrow p\pi^+\pi^-$ was used to tune the covariance matrix in order to secure Gaussian pull distributions and a flat confidence-level (CL) distribution,

where the confidence level denotes the goodness of fit to the data and is defined as the integral over the χ^2 probability density function in the range $[\chi^2, \infty]$ [34]. Figure 5 shows confidence-level distributions for the missing- π^0 hypothesis before (dashed-blue line) and after (solid-black line) all corrections. Events in this analysis were retained with a confidence-level cut of $p > 0.001$.

B. Background subtraction

Frozen beads of butanol (C_4H_9OH) were used for the target material. When these butanol beads were polarized, only the 10 *free* hydrogen nucleons of the butanol could be polarized. Meson photoproduction on bound nucleons in ^{12}C and ^{16}O nuclei nonetheless generate a background beneath the signal from the polarized free nucleons. Owing to Fermi motion and final-state interactions, signals from reactions off ^{12}C and ^{16}O nucleons are broadened such that those signals do not form discernible peaks in the mass distributions. Although this background contribution drops out in the numerator of Eq. (2), the contribution from bound nucleons still remains in the denominator, requiring a procedure to remove any effects from that bound-nucleon contribution. Commonly, a dilution factor is calculated to account for the bound-nucleon contributions to the normalization in Eq. (2), defined as the ratio of the free-proton contribution to the full butanol cross section. The energy- and angle-dependent effective dilution factors are usually determined from mass distributions obtained from measurements on additional targets (such as the carbon and CH_2 disk targets mentioned above in Sec. III). However, in the measurements of the ω helicity asymmetry reported

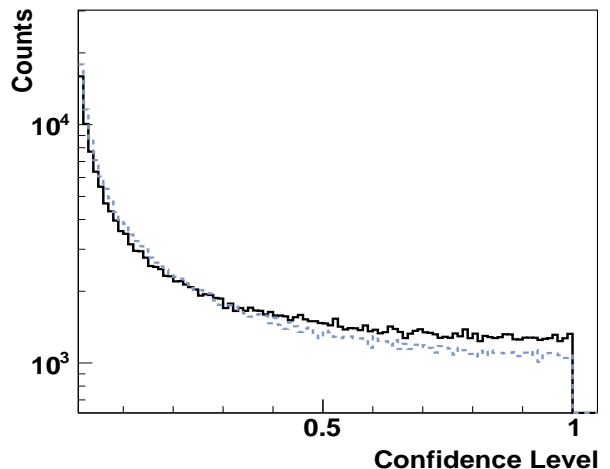


FIG. 5. (Color online) Confidence-level distribution for a one-constraint (1C) fit testing events for a missing π^0 . The blue-dashed line is based on *raw* events, whereas the black-solid line is based on the final event sample after all corrections.

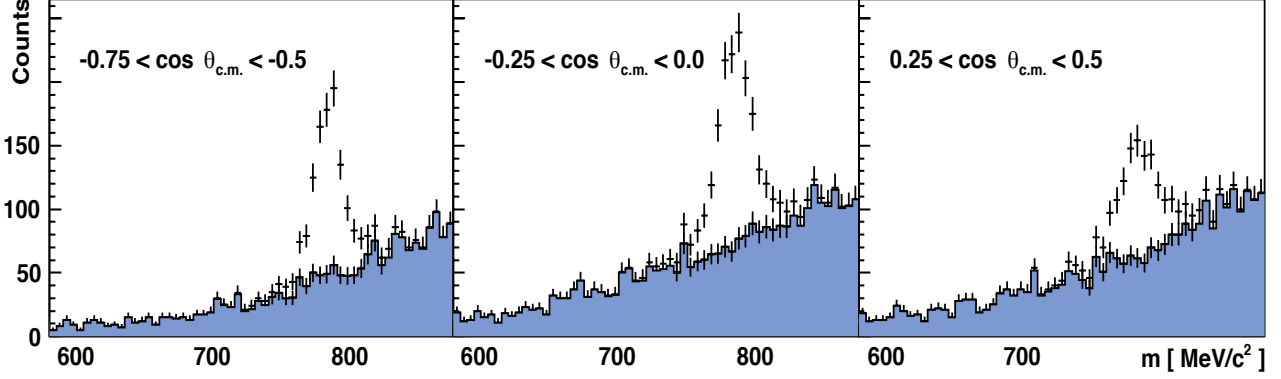


FIG. 6. (Color online) Examples of invariant $\pi^+\pi^-\pi^0$ mass distributions in the photon energy range $E_\gamma \in [1.5; 1.6]$ GeV for events that were subjected to the Q -factor fitting (background subtraction). These events survived all kinematic cuts. The solid blue area indicates the background.

here, non-signal background events were removed in a probabilistic event-based approach called the “ Q -factor method,” described briefly here and detailed more fully in Ref. [35]. That method was used for subtracting the background from the bound nucleons in the carbon and oxygen content of the butanol, as well as the removal of other sources of background.

The method assigns a quality factor (or Q factor) to each event. These factors effectively serve as event-based dilution factors and describe the probability for an event to be a signal event. The Q factors were then used to weight each event in the analysis when the observable was extracted. The method is a generalization of the traditional one-dimensional side-band subtraction method to higher dimensions without binning the data. Figure 6 shows examples of the resulting separation of signal and background in the invariant $\pi^+\pi^-\pi^0$ mass distribution. Three angle bins are presented in the energy range $E_\gamma \in [1.5; 1.6]$ GeV. The sum of the signal (white area) and the background (blue area) is identical to the total unweighted mass distribution, whereas the invariant 3π mass of each event weighted by $1 - Q$ gives the background alone.

In this event-based method, the general set of coordinates that describe the multi-dimensional phasespace of a reaction is separated into *reference* and *non-reference* coordinates. In this analysis, the invariant $M_{\pi^+\pi^-\pi^0}$ mass was chosen as the reference coordinate. The Q -factor method proceeded with the selection of the N_c kinematically-nearest neighbors for each event. A number of $N_c = 300$ was chosen by defining a distance metric for the individual kinematic variables spanning the phase space:

$$D_{ab}^2 = \sum_{i=1}^5 \left(\frac{\Gamma_i^a - \Gamma_i^b}{\Delta_i} \right)^2, \quad (5)$$

where the Γ_i denote the set of kinematic variables for the two events a and b , and Δ_i is the full range for the

kinematic variable i . The following independent non-reference variables were used:

$$\cos \theta_{\text{c.m.}}^\omega, \cos \theta_{\text{HEL}}, \phi_{\text{HEL}}, \phi_{\text{lab}}^\omega, \lambda, \quad (6)$$

where $\cos \theta_{\text{c.m.}}^\omega$ denotes the cosine of the polar angle of the ω in the center-of-mass frame, $\cos \theta_{\text{HEL}}$ and ϕ_{HEL} are the two angles of the ω in the helicity frame, and ϕ_{lab}^ω is the azimuthal angle of the ω in the laboratory frame. Defined in terms of the pion momenta in the ω rest frame, the variable $\lambda = |\vec{p}_{\pi^+} \times \vec{p}_{\pi^-}|^2 / \lambda_{\text{max}}$ is proportional to the $\omega \rightarrow \pi^+\pi^-\pi^0$ decay amplitude as a consequence of isospin conservation [13], with λ_{max} defined as [36]

$$\lambda_{\text{max}} = Q^2 \left(\frac{Q^2}{108} + \frac{mQ}{9} + \frac{m^2}{3} \right) \quad (7)$$

for a totally symmetric decay, where $Q = T_1 + T_2 + T_3$ is the sum of the $\pi^{\pm,0}$ kinetic energies and m is the π mass. The parameter λ varies between 0 and 1 and shows a linearly-increasing distribution as expected for a vector meson. Event-based maximum likelihood fits were performed of the invariant $M_{3\pi}$ distributions for every selected event and its N_c nearest neighbor events according to:

$$f(x) = N \cdot [f_s \cdot S(x) + (1 - f_s) \cdot B(x)], \quad (8)$$

where $S(x)$ and $B(x)$ denote the signal and the background probability density functions, respectively, and $x = M_{3\pi}$. A Voigt profile was chosen for the signal and the background shape was modeled with a second-order Chebychev polynomial. The parameter N was a normalization constant and f_s was the signal fraction with a value between 0 and 1. The Q factor is defined by:

$$Q = \frac{s(x)}{s(x) + b(x)}, \quad (9)$$

where x is again the invariant mass of the $\pi^+\pi^-\pi^0$ system, $s(x) = f_s \cdot S(x)$, and $b(x) = (1 - f_s) \cdot B(x)$.

V. EXTRACTION OF THE E OBSERVABLE

Data using an unpolarized- or a circularly-polarized photon beam in combination with an unpolarized- or a longitudinally-polarized target are isotropic in the laboratory azimuthal angle since the orientation of any particle polarization is along the z -axis in the laboratory frame. Any polarization asymmetry for a kinematic bin is given by the difference in the event counts for parallel/anti-parallel polarization settings:

$$A^{\Rightarrow} = \frac{N_{\rightarrow\rightarrow}^{\Rightarrow} - N_{\rightarrow\leftarrow}^{\Rightarrow}}{N_{\rightarrow\rightarrow}^{\Rightarrow} + N_{\rightarrow\leftarrow}^{\Rightarrow}} = A^{\Leftarrow} = \frac{N_{\leftarrow\rightarrow}^{\Leftarrow} - N_{\leftarrow\leftarrow}^{\Leftarrow}}{N_{\leftarrow\rightarrow}^{\Leftarrow} + N_{\leftarrow\leftarrow}^{\Leftarrow}}, \quad (10)$$

where \rightarrow (\leftarrow) and \Rightarrow (\Leftarrow) indicate if the photon and nucleon spin points downstream (upstream), respectively.

The corresponding polarization observable can then be extracted from this asymmetry and Eq. (2) reduces to:

$$E = \frac{1}{\Lambda_z^{\Rightarrow} \delta_{\odot}} A^{\Rightarrow} = \frac{1}{\Lambda_z^{\Leftarrow} \delta_{\odot}} A^{\Leftarrow}, \quad (11)$$

where δ_{\odot} denotes the degree of circular photon-beam polarization and Λ_z is the degree of longitudinal target-proton polarization

VI. EXPERIMENTAL RESULTS

The kinematics of ω photoproduction from the proton can be completely described by two kinematic variables. The incoming photon energy E_{γ} and $\cos\theta_{\text{c.m.}}^{\omega}$ were chosen, where $\theta_{\text{c.m.}}^{\omega}$ is the polar angle of the photoproduced ω in the center-of-mass frame. The z -axis was defined as the direction of the incident photon beam.

A. The E observable for $\gamma p \rightarrow p\omega$

Figure 7 shows the E observable for the photoproduction of a single- ω meson off the proton from this analysis (red circles \bullet). The angular distributions are shown for 100-MeV-wide bins in the incoming photon energy. Figure 8 shows the energy dependence of the E observable for eight angle bins in $\cos\theta_{\text{c.m.}}^{\omega}$. For comparison, earlier results from the CBELSA/TAPS Collaboration [21] are also shown (blue boxes \blacksquare) in Figs. 7 and 8. Both data sets are consistent in their asymmetry behavior (same sign for almost every data point). However, larger discrepancies in the magnitude are visible, in particular at low energies, $E_{\gamma} < 1.5$ GeV.

In an effort to resolve these discrepancies, we identified three likely sources: (1) beam polarization, (2) target polarization, and (3) background subtraction (see also Eqs. (10) and (11)). The values for the accelerator-beam polarization and the target polarization used in this analysis are the same as those values applied in the extraction of the η helicity asymmetry at CLAS described in Ref. [32]. This CLAS- η analysis was based on

the same FROST data set as the ω analysis presented here. The η observable showed the expected flat behavior close to the reaction threshold and a magnitude of almost one owing to the dominance of the $N(1535) 1/2^{-}$ nucleon resonance. Moreover, the mass distributions presented in Fig. 6, which refer to the incident-photon energy range [1.5, 1.6] GeV (see Fig. 7), do not indicate that our background-subtraction technique is the major cause for the observed discrepancy between the CLAS and the CBELSA/TAPS results in this energy range. We note that a possible overestimation of the $\omega \rightarrow \pi^0\gamma$ yields at ELSA may be the origin of the inconsistency between the two data sets. For the radiative decay of the ω , the reactions $\gamma p \rightarrow p\pi^0\pi^0$ (with one low-energy photon undetected) and $\gamma p \rightarrow p\pi^0$ (with an additional photon misrepresented), exhibit “peaking” background close to the ω in the invariant $\pi^0\gamma$ mass distribution, which is very challenging to account for. We refer to Refs. [14, 21] for more details on the techniques of analyzing the reaction $\gamma p \rightarrow p\omega \rightarrow p\pi^0\gamma$.

B. Systematic uncertainties

The statistical uncertainties were determined from the number of events in each $(E_{\gamma}, \cos\theta_{\text{c.m.}}^{\omega})$ bin and are shown for all data points in Figs. 7 and 8; systematic uncertainties are given as bands at the bottom of each distribution.

The overall systematic uncertainty includes uncertainties in the degree of photon-beam and target-proton polarization, contributions from the electron-beam charge asymmetry, and the background-subtraction method. The systematic uncertainties in the degree of photon-beam and target-proton polarization are applied as global factors of 2 % and 3 %, respectively. Other sources of systematic uncertainty are described below.

The electron-beam polarization was toggled between the h^{+} and the h^{-} helicity states at a rate of 29.560 Hz. At these large rates, the photon-beam flux for both helicity states should be the same, on average. However, small beam-charge asymmetries of the electron beam can cause instrumental asymmetries and lead to systematic deviations in the hadronic asymmetries. The electron beam-charge asymmetry was calculated from the luminosities of h^{+} and h^{-} events:

$$\Gamma^{\pm} = \alpha^{\pm} \Gamma = \frac{1}{2} (1 \pm \bar{a}_c) \Gamma, \quad (12)$$

where Γ was the total luminosity and α^{\pm} denoted the fraction of h^{+} and h^{-} events. The parameter α^{\pm} depended on the mean value of the electron beam-charge asymmetry, \bar{a}_c , which was typically less than 0.2 %. Therefore, contributions from this source of the systematic uncertainty were considered negligible.

The Q -factor method will lead to a certain level of correlation among events because events can share a significant number of the same neighbors in the limit of

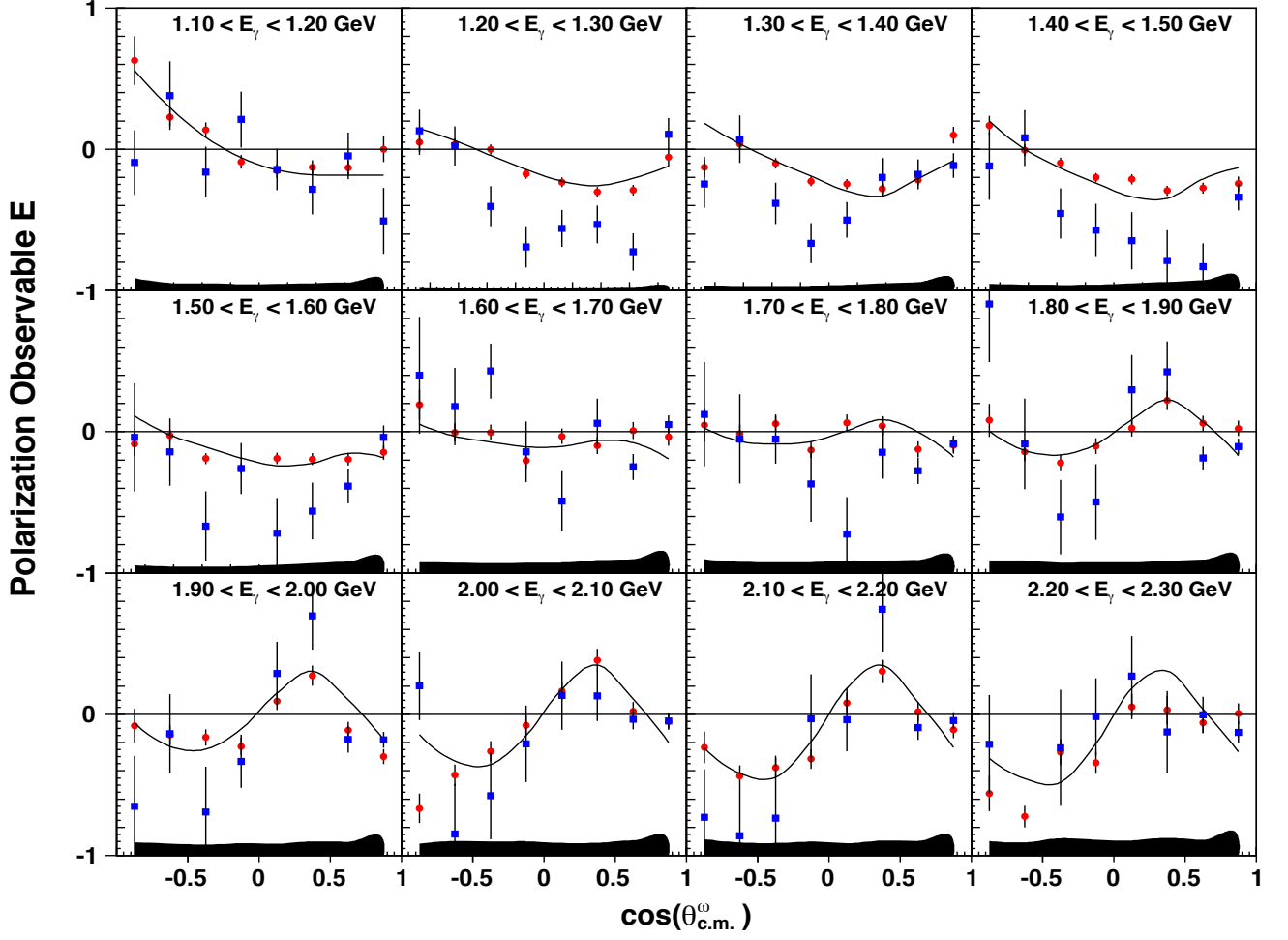


FIG. 7. (Color online) Measurement of the helicity asymmetry E in the reaction $\gamma p \rightarrow p\omega$ using a circularly-polarized photon beam and a longitudinally-polarized target. The data are shown in 100-MeV-wide bins for the photon energy range $E_\gamma \in [1.1, 2.3]$ GeV. The CLAS-FROST results (red circles \bullet) are compared with results from the CBELSA/TAPS Collaboration [21], which used the radiative decay mode, $\omega \rightarrow \pi^0\gamma$ (blue squares \blacksquare). The black solid line represents the BnGa PWA solution. The data points include statistical uncertainties only; the total systematic uncertainty is given as bands at the bottom of each distribution.

very small statistics. For this reason, the systematic uncertainty in the ω yield in a kinematic bin due to the Q -factor method was obtained from the covariance matrix of each fit and the correlation factors between events i and j , which describe the fraction of shared nearest neighbor events between two events. The systematic variance is given by

$$\sigma_\omega^2 = \sum_{i,j} \sigma_Q^i \rho_{ij} \sigma_Q^j, \quad (13)$$

where the sum i, j extends over all events in a kinematic $(E_\gamma, \cos \theta_{\text{c.m.}})$ bin, σ_Q^i and σ_Q^j are the fit uncertainties for events i and j , and ρ_{ij} is the correlation factor between events i and j . The absolute uncertainties due to the Q -factor method range from about 0.03 close to the reaction threshold to about 0.1 at $E_\gamma = 2$ GeV.

An additional possible source of systematic uncertainty is the presence of accidental photons. The fraction of

accidental photons was at most 2.5%. It was estimated from comparing the central peak with the neighboring electron beam buckets in the *coincidence-time* spectrum, which is defined per photon as the difference between the Tagger time and the Start Counter time at the interaction point. Accidental photons lead to an overestimation of the event numbers but drop out in the asymmetry of event counts.

VII. PARTIAL-WAVE ANALYSIS

Baryon resonances are very short-lived and as a result, these states are broad and overlapping. Contributions from resonances manifest themselves as enhancements or peak-like structures in the cross sections. Owing to the broad nature of baryon resonances however, peaks in the experimental cross sections are typically based on

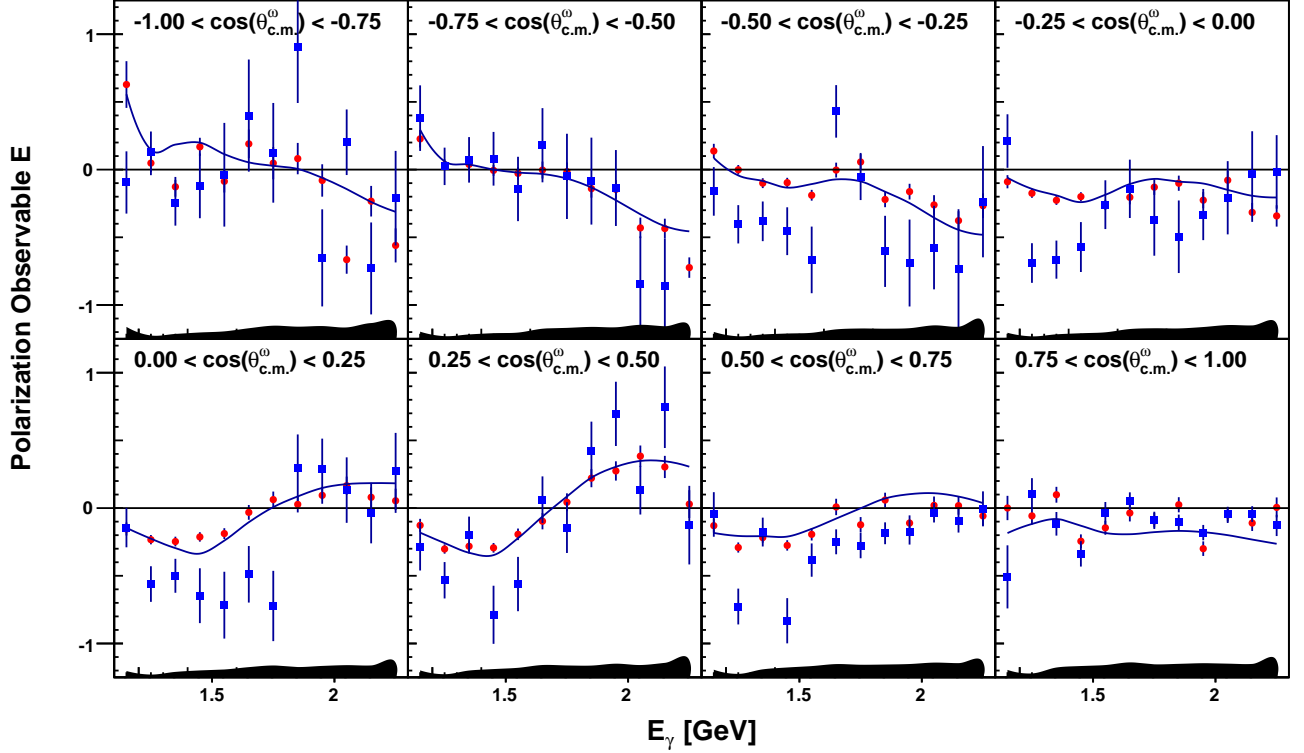


FIG. 8. (Color online) Measurement of the helicity asymmetry E in the reaction $\gamma p \rightarrow p\omega$ using a circularly-polarized photon beam and a longitudinally-polarized target. The data are shown in 0.25-wide-bins in $\cos \theta_{\text{c.m.}}^\omega$ and in 100-MeV-wide bins for the photon energy range $E_\gamma \in [1.1, 2.3]$ GeV. The CLAS-FROST results (red circles \bullet) are compared with results from the CBELSA/TAPS Collaboration [21], which used the radiative decay mode, $\omega \rightarrow \pi^0\gamma$ (blue squares \blacksquare). The black solid line represents the BnGa PWA solution. The data points include statistical uncertainties only; the total systematic uncertainty is given as bands at the bottom of each distribution.

contributions from many resonances and can merely be addressed as resonance regions. Extracting N^* parameters from the data thus remains a challenge. Amplitude analyses or PWAs need to be performed in order to identify resonance contributions in a particular reaction. The situation becomes more complicated at higher resonance masses because many reaction channels need to be considered. Any reliable extraction of resonance properties must therefore be based on a coupled-channels approach.

In recent years, several groups have contributed significantly to our understanding of the baryon spectrum, but a comprehensive analysis based on a large database of observables has been performed only at a few institutions, see e.g. Refs. [16, 37] and references therein. The precise photoproduction data resulting from recent experiments have a great significance for the extraction of baryon resonance parameters. In particular, the data on some polarization observables are decisive in avoiding ambiguities in the description of resonance contributions.

This section describes the results of a PWA in the framework of the BnGa coupled-channels approach that is based on the new $\gamma p \rightarrow p\omega$ data from CLAS on the polarization observables E (presented here), T and Σ [19, 20], and F , P , and H [38]. The CLAS data were

added to the full BnGa database, which includes a large set of data on pion- and photo-induced meson-production reactions, with up to two pseudoscalar mesons in the final state [39]. The BnGa group has recently reported on a PWA [8] that, at the time, was restricted to ω data from the CBELSA/TAPS experiment alone: (1) Differential cross sections and spin-density matrix elements (SDMEs) for unpolarized incident photons ($\rho_{00}^0, \rho_{10}^0, \rho_{1-1}^0$) covering the energy range from threshold to 2500 MeV, as well as SDMEs for linearly-polarized incident photons ($\rho_{00}^1, \rho_{11}^1, \rho_{1-1}^1, \rho_{10}^2, \rho_{10}^2, \rho_{1-1}^2$) covering the energy range $E_\gamma < 1650$ MeV [14]; (2) Data on the photon-beam asymmetry Σ [18]; (3) Results on the helicity asymmetry, E , ($E_\gamma < 2300$ MeV) and the G observable for one bin in photon energy ($1108 < E_\gamma < 1300$ MeV) [21].

The new BnGa-PWA solution, which is based on the CLAS data, is shown in Fig. 7 and 8 as a solid line. More details on the PWA and branching ratios for N^* decays into $N\omega$ will be discussed in a subsequent publication [40]. The inclusion of SDMEs allowed the study of the ω production process in more detail and helped separate the natural and unnatural parity-exchange contributions. In the BnGa analysis, π exchange in the t -channel was found to remain small across the analyzed

energy range, while pomeron t -channel exchange gradually grew from the reaction threshold to dominate all other contributions above $W \approx 2$ GeV ($E_\gamma > 1.66$ GeV).

In the BnGa analysis, close to the reaction threshold, $J^P = 3/2^+$ remains the leading resonant partial wave and shows a strong peak with a maximum around $W = 1.8$ GeV. This wave is identified with the $N(1720) 3/2^+$ state, which is situated just below the reaction threshold. The $3/2^+$ partial wave has a more complex structure and indications for at least one more resonance around $W = 1.9$ GeV have been found. The contributions from the $1/2^-$ and $3/2^-$ partial waves are notably smaller compared to the leading $3/2^+$ partial wave. The $J^P = 1/2^-$ wave has a maximum close to the reaction threshold, which can be identified with the $N(1895) 1/2^-$ resonance, and smoothly declines toward higher masses; no further structures are observed. The $J^P = 3/2^-$ wave reaches a maximum just above 2 GeV, which can be identified with contributions from the $N(2100) 3/2^-$ state. The $J^P = 5/2^+$ wave exhibits a richer structure. This wave has a local enhancement close to the threshold, identified with $N(1680) 5/2^+$, and a maximum around $W = 2$ GeV; the latter is identified with the poorly-established $N(2000) 5/2^+$ state. The $N\omega$ coupling of this resonance has significantly increased compared to the previous BnGa ω PWA. The contributions from the $5/2^-$, $7/2^+$, and $7/2^-$ partial waves remain smaller. In all fits, they were found to be less than about 5%. The $7/2$ partial waves play an important role in the description of the density matrices at masses above 2.1 GeV.

VIII. SUMMARY

The double-polarization observable E for the reaction $\gamma p \rightarrow p \omega$ has been measured at CLAS using the frozen-

spin FROST target, covering the energy range from 1.1 to 2.3 GeV using the $\omega \rightarrow \pi^+ \pi^- \pi^0$ decay. Fairly large helicity asymmetries are observed, indicating significant contributions from s -channel N^* resonances. The data have been partial-wave analyzed within the BnGa coupled-channels framework and contributions from N^* resonances have been identified. The leading partial waves at the reaction threshold are the $3/2^+$ and $5/2^+$ waves. Toward higher energies around $W \approx 2$ GeV, the t -channel contributions increase in strength and are defined by a dominant pomeron exchange and a smaller π exchange. In addition, further contributions from nucleon resonances are required to describe the data. The $1/2^-$, $3/2^-$, and $5/2^+$ partial waves show considerable contributions to the PWA solution.

ACKNOWLEDGMENTS

The authors thank the technical staff at Jefferson Lab and at all the participating institutions for their invaluable contributions to the success of the experiment. This material is based upon work supported by the U.S. Department of Energy, Office of Science, Office of Nuclear Physics, under Contract No. DE-AC05-06OR23177. This work was also supported by the US National Science Foundation, the State Committee of Science of Republic of Armenia, the Chilean Comisión Nacional de Investigación Científica y Tecnológica (CONICYT), the Italian Istituto Nazionale di Fisica Nucleare, the French Centre National de la Recherche Scientifique, the French Commissariat à l'Energie Atomique, the Scottish Universities Physics Alliance (SUPA), the United Kingdom's Science and Technology Facilities Council, the National Research Foundation of Korea, the Deutsche Forschungsgemeinschaft (SFB/TR110), and the Russian Science Foundation under Grant No. 16-12-10267.

-
- [1] H. Al Ghoul *et al.* [GlueX Collaboration], Phys. Rev. C **95**, no. 4, 042201 (2017).
 - [2] A. Donnachie and P. V. Landshoff, Phys. Lett. B **348**, 213 (1995).
 - [3] J. Ballam *et al.*, Phys. Rev. D **7**, 3150 (1973).
 - [4] J. Abramson *et al.*, Phys. Rev. Lett. **36**, 1428 (1976).
 - [5] D. P. Barber *et al.* [LAMP2 Group], Z. Phys. C **26**, 343 (1984).
 - [6] J. M. Laget, Nucl. Phys. A **699**, 184 (2002).
 - [7] A. Sibirtsev, K. Tsushima and S. Krewald, Phys. Rev. C **67**, 055201 (2003).
 - [8] I. Denisenko *et al.*, Phys. Lett. B **755**, 97 (2016).
 - [9] M. Williams *et al.* [CLAS Collaboration], Phys. Rev. C **80**, 065209 (2009).
 - [10] Q. Zhao, Phys. Rev. C **63**, 025203 (2001).
 - [11] J. Barth *et al.*, Eur. Phys. J. A **18**, 117 (2003).
 - [12] J. Ajaka *et al.*, Phys. Rev. Lett. **96**, 132003 (2006).
 - [13] M. Williams *et al.* [CLAS Collaboration], Phys. Rev. C **80**, 065208 (2009).
 - [14] A. Wilson *et al.* [CBELSA/TAPS Collaboration], Phys. Lett. B **749**, 407 (2015).
 - [15] I. I. Strakovsky *et al.*, Phys. Rev. C **91**, no. 4, 045207 (2015).
 - [16] V. Crede and W. Roberts, Rept. Prog. Phys. **76**, 076301 (2013).
 - [17] V. Vigna *et al.* [GRAAL Collaboration], Phys. Rev. C **91**, no. 6, 065207 (2015).
 - [18] F. Klein *et al.* [CBELSA/TAPS Collaboration], Phys. Rev. D **78**, 117101 (2008).
 - [19] P. Collins *et al.*, Phys. Lett. B **773**, 112 (2017).
 - [20] P. Roy *et al.* [CLAS Collaboration], arXiv:1711.05176 [nucl-ex].
 - [21] H. Eberhardt *et al.*, Phys. Lett. B **750**, 453 (2015).
 - [22] B. A. Mecking *et al.*, Nucl. Instrum. Meth. A **503**, 513 (2003).
 - [23] C. D. Keith *et al.*, Nucl. Instrum. Meth. A **684**, 27 (2012).
 - [24] H. Olsen and L. C. Maximon, Phys. Rev. **114**, 887 (1959).

- [25] R. Nasseripour *et al.*, Bull. Am. Phys. Soc. **45**, 91 (2000);
B. A. Raue *et al.*, Bull. Am. Phys. Soc. **43**, 1543 (1998).
- [26] D. I. Sober *et al.*, Nucl. Instrum. Meth. A **440**, 263 (2000).
- [27] M. D. Mestayer *et al.*, Nucl. Instrum. Meth. A **449**, 81 (2000).
- [28] E. S. Smith *et al.*, Nucl. Instrum. Meth. A **432**, 265 (1999).
- [29] Y. G. Sharabian *et al.*, Nucl. Instrum. Meth. A **556**, 246 (2006).
- [30] A. Abragam and M. Goldman, Rep. Prog. Phys. **41**, 395 (1978).
- [31] S. Strauch *et al.* [CLAS Collaboration], Phys. Lett. B **750**, 53 (2015).
- [32] I. Senderovich *et al.* [CLAS Collaboration], Phys. Lett. B **755**, 64 (2016).
- [33] C. Patrignani *et al.* [Particle Data Group], Chin. Phys. C **40**, no. 10, 100001 (2016).
- [34] S. Brandt, *Data Analysis* (Springer-Verlag New York, 1999), ISBN 0-387-98498-4.
- [35] M. Williams, M. Bellis and C. A. Meyer, J. Instrum. **4**, P10003 (2009).
- [36] P. Weidenauer *et al.* [ASTERIX Collaboration], Z. Phys. C **59**, 387 (1993).
- [37] E. Klempt and J. M. Richard, Rev. Mod. Phys. **82**, 1095 (2010).
- [38] P. Roy *et al.* [CLAS Collaboration] (unpublished).
- [39] http://pwa.hiskp.uni-bonn.de/baryon_x.htm
- [40] A. V. Anisovich *et al.* (unpublished).